ACS APPLIED NANO MATERIALS

www.acsanm.org Article

Silica Nanoparticles Synthesized from 3,3,3-Propyl(trifluoro)trimethoxysilane or *n*-Propyltrimethoxysilane for Creating Superhydrophobic Surfaces

Abul Bashar Mohammad Giasuddin, Anthony Cartwright, and David W. Britt*

Cite This: *ACS Appl. Nano Mater.* 2021, 4, 4092−4102 Read Online

ACCESS | Metrics & More | Article Recommendations | Supporting Information

ABSTRACT: Superhydrophobic silica (SHS) nanoparticles (NPs) with fluoro- or alkyl-surface functionalization are explored for a wide range of potential applications. Here, the aqueous synthesis of SHS NPs from single precursors, 3,3,3-propyl(trifluoro)-trimethoxysilane (3F) and *n*-propyltrimethoxysilane (*n*PM), are presented. The 3F and *n*PM precursor silanes were solubilized by acid hydrolysis followed by base condensation to synthesize NPs ranging from 50 to 300 nm, dependent on silane concentration. Dynamic light scattering and atomic force microscopy revealed that NP size decreased with precursor concentrations. The 3F NPs displayed lower size, polydispersity, and surface roughness compared to *n*PM NPs synthesized at the same precursor concentrations, indicating distinct sol−gel kinetics for the two hydrophobic silanes. Attenuated total reflection-Fourier transform infrared spectroscopy revealed free silanol groups on fluoro-NPs and powder X-ray diffraction showed distinct peak intensities for fluoro- and alkyl-NPs supporting a greater propensity toward fully condensed oligomeric silsesquioxane (POSS) cage structures for *n*PM than for 3F. Space-filling models attributed these structural differences to steric constraints of the terminal CF_3 moiety on 3F contrasted with CH_3 on *n*PM. A difunctional analog of 3F was unable to assemble into particles during the condensation process, supporting the role of POSS cages as the fundamental assembly unit. Both NPs formed superhydrophobic thin films demonstrating water contact angles >165° and sliding angles <5°. The aqueous synthesis of SHS NPs from either fluoro- or organo-silane single-source precursors provides alternative pathways to constructing SHS NPs for applications requiring superhydrophobicity.

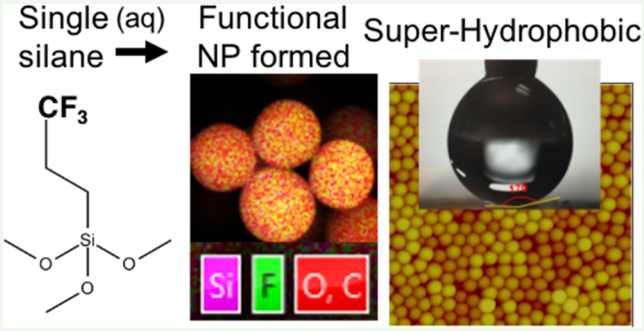

KEYWORDS: *superhydrophobic, fluoro-silica, organo-silica, nanoparticles, oligomeric silsesquioxanePOSS, organically modified silica, ORMOSIL*

INTRODUCTION

Silica nanoparticles (NPs) are widely used in biomedical,[1,2] food,[3] electronics,[4] and chemical[5−7] industries due to their high surface area, thermal and chemical stability, optical transparency, functionalizing ability with a wide range of molecules and polymers, biocompatibility, and scalable synthetic availability. Silica NPs are produced following both gaseous and liquid routes, with sol−gel chemistry being most commonly used.[8] The sol−gel synthesis generally follows the Stöber method where alkoxysilanes such as tetraethoxysilane (TEOS) or tetramethoxysilane (TMOS) undergo stepwise hydrolysis and polycondensation to form colloids.[9] The Stöber method has been tuned through modifications to silane concentrations, solvent conditions, catalysts, and temperatures to better control silica NP growth and the resulting particle sizes.[10−13] Alkoxysilanes with various organo-functionalities are also used to modify silica NP properties by cocondensing them with a core silane precursor as well as postfunctionalizing them on presynthesized silica NPs to produce ORMOSILs.[14−16]

Silica NPs with organo- or fluoro-functionality are often used in coatings to achieve superhydrophobic surfaces as they also exhibit high thermal and mechanical stability, low surface energy, and tunable surface roughness.[17−22] A surface is considered superhydrophobic when the water forms a contact angle larger than 150° and the sliding angle is lower than 5°.[23] Such extremely water repellent surfaces continue to attract interest given their potential applications, including toners, self-cleaning/nonfouling materials, anticorrosion, antifogging, anti-icing coatings, waterproof textiles, drag reduction, and oil−water separation applications.[24−33] To render a surface superhydrophobic, a combination of micro-to-nano roughness and

Received: February 7, 2021
Accepted: March 10, 2021
Published: March 22, 2021

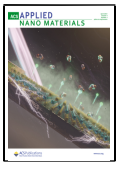

https://doi.org/10.1021/acsanm.1c00398
ACS Appl. Nano Mater. 2021, 4, 4092−4102

Table 1. Summary of Conventional Syntheses of SHS NPs[a]

method	precursor name	precursor no./ step	solvent	reaction temperature (°C)	ref
functionalization	trimethoxy(octadecyl)silane	2	toluene	90	25
Stöber + functionalization	TEOS, PFOTS, CTAB	3	IPA and water	70	36
Stöber + functionalization	TEOS, trimethyl(fluoromethyl)silane, AIBN, CTAB, styrene	3	water, *n*-octane	60	37
Stöber + cocondensation + functionalization	TEOS, APTES, dibutyltindilaurate, and IPDI	3	ethanol and butyl acetate (BuA)	70−75	39
functionalization	dodecyltrichlorosilane	2	ethanol, toluene	23	40
Stöber + functionalization	TEOS, SDBS, hexadecyltrimethoxysilane		water, ethanol	60	42
microwave + functionalization	hexadecyltrimethoxysilane	2	ethanol	50	44
Stöber + functionalization	TEOS, ethanolilc fluoroalkylsilane	2	ethanol	50	45

[a]TEOS: tetraethoxysilane, APTES: triethoxysilane, IPDI: isophorone diisocyanate, CTAB: cetyltriammonium bromide, PFOTS: 1H,1H,2H,2H-perfluorooctytriethoxisilane SDBS: sodium dodecylbenzenesulfonate, and AIBN: azobisisobutyronitrile.

low interfacial energy is required.[34] Application of hydrophobic microparticles with nanoscale features or using nanoparticles to coat a surface with microtopography both yield superhydrophobicity. Superhydrophobic silica nanoparticles are typically derived by postfunctionalizing silica particles with hydrophobic silanes, which often leads to partial hydrophobic surface coverage. Here, a single hydrophobic silane precursor is used to construct both the core nanoparticle and hydrophobic surface, reducing the number of steps and components.

Both organo and fluoro moieties are employed in rendering silica superhydrophobic. Fluorocarbon-based low-surface-energy precursors such as fluoro-silanes are used to functionalize silica NPs to achieve superhydrophobic surfaces.[35−38] However, fluorine-free alkyl-silanes with low surface energies have also been explored to render NP surface superhydrophobic.[39−44] The conventional synthesis of both fluoro- and alkyl-functionalized superhydrophobic silica (SHS) NPs requires multiple precursors and a multistep process. Initially, silica NPs would be synthesized from alkoxysilane or sodium silicate as the precursor followed by the incorporation of fluoro- or hydrocarbon functionalities from these respective silane precursors in a cocondensation or surface functionalization process, as shown in Table 1.

For example, Sriramulu et al. prepared SHS NPs by functionalizing trimethoxy(octadecyl)silane on presynthesized silica NPs.[25] Similarly, Brassard et al. synthesized silica NPs first following Stöber methods using TEOS and then added ethanolic fluoroalkylsilane ($C_{16}H_{19}F_{17}O_3Si$) to achieve superhydrophobic properties.[45] Ye et al. prepared fluorine-free SHS NPs by adding isophorone diisocyanate on (3-aminopropyl) triethoxysilane (APTES)-modified silica NPs formed by cocondensing APTES and TEOS.[39]

Conventionally, both the synthesis and the hydrophobic functionalization of silica NPs are performed in organic solvents.[35,36,39,40,45−47] The use of organic solvents not only introduces flammable and toxic compounds during synthesis but also increases the economic and environmental burden to the process as solvent recovery/disposal requires further steps in the postprocessing stage. Lee et al. reported the aqueous synthesis of silica particles from a single precursor, but the synthesized particles are micro-sized and the surface properties of the particles such as hydrophobicity were not reported.[48] Hu et al. also synthesized silica colloids in an aqueous solvent but used salt/surfactant templates along with the silane precursors and make no mention of surface properties.[49]

Here, we report an aqueous method using mild acid (HCl) followed by the addition of a base (NH_4OH) to synthesize SHS NPs with either fluoro- or alkyl-functionality, 3,3,3-propyl-(trifluoro)trimethoxysilane (3F) and *n*-propyltrimethoxysilane (*n*PM), respectively, directly from single silane precursors at room temperature. Acid assists in hydrolyzing and solubilizing the hydrophobic precursors, while the base catalyzes particle formation. Without the base, hydrolyzed silanes condense to form colloidal silica that aggregates into gels. The acid hydrolysis step allows for a complete solubilization of the precursor but requires a base catalyst. Dixit et al. demonstrated an elegant approach using just a base catalyst in a water/alcohol solvent in which they eliminated unreacted TEOS precursor using a "phasing out" emulsification process in water.[12,13] This method has been extended to a single-pot synthesis of a TEOS core NP followed by continued growth through the introduction of epoxy silane, resulting in a composite NP with epoxy silane surface chemistry.[16] Here, the use of a single hydrophobic precursor ensures a 1:1 stoichiometry of hydrophobic functionality to Si, which is not possible in the conventional synthesis of SHS NPs by a two-step process of silica NP synthesis followed by coating with a hydrophobic alkyl- or fluoroalkylsilane. This high degree of hydrophobic functionality is reflected in water contact angles above 160° for thin films of the alkyl- and fluoro-NPs. Network polymerization is supported for both *n*PM and 3F based on infrared spectroscopy, X-ray diffraction, and the inability of a difunctional (diethoxy) analog of 3F to form spherical NPs. A growth model of seed particle formation is supported by dynamic light scattering and atomic force microscopy, with size ranges between 50 and 300 nm readily controlled by precursor concentrations. To our knowledge, this is the first report on the aqueous and controlled synthesis of fluorinated and alkylated SHS NPs from single-source silane precursors.

EXPERIMENTAL SECTION

Materials. All chemicals were used as received. (3,3,3-Trifluoropropyl)trimethoxysilane (3F, >95% purity, MW = 218.3, ρ = 1.14 g mL^{-1}), (3,3,3-trifluoropropyl)methyldimethoxysilane (D3F, >95% purity, MW = 202.25, ρ = 1.089 g mL^{-1}), and *n*-propyltrimethoxysilane (*n*PM, >95% purity, MW = 164.3, ρ = 0.94 g mL^{-1}) were purchased from Gelest, Inc. (Morrisville, PA). Ammonium hydroxide, 50% v/v, was purchased from LabChem Inc. (Pittsburgh, PA). Muscovite mica was purchased from SPI supplies (PA). Hydrochloric acid (1 N HCl) was purchased from RICCA chemical company. Double-distilled water (DDI) with a resistivity >18 MΩ·cm was obtained from a Barnstead Mega-Pure system (MP-3A, ACS unit).

Synthesis of Fluoro- and Alkyl-Silica NPs. The 3F (0.4 M) and *n*PM (0.4 M) silanes were hydrolyzed in mildly acidic double-distilled-deionized (DDI) water (pH adjusted to 3.0 with 1 N HCl) in separate

https://doi.org/10.1021/acsanm.1c00398
ACS Appl. Nano Mater. 2021, 4, 4092−4102

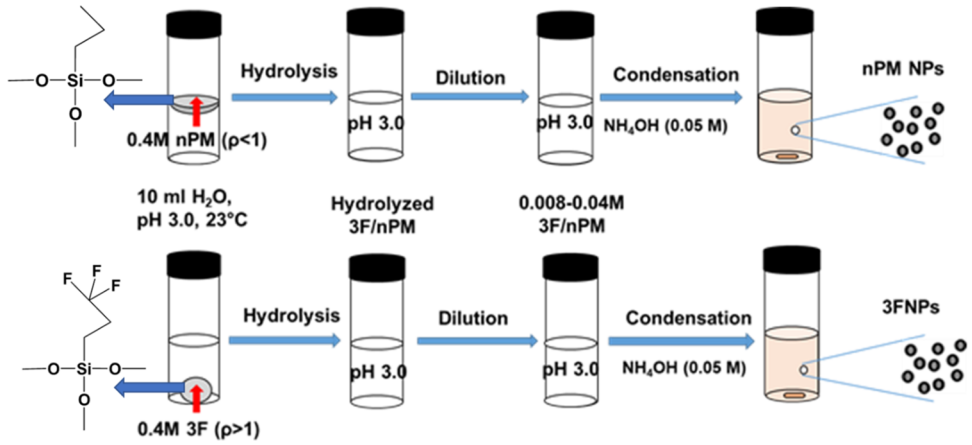

Figure 1. Experimental schematic for fluoro-silane (bottom) and alkyl-silane (top) nanoparticle synthesis. The completion of acid-catalyzed hydrolysis is confirmed by the disappearance of the immiscible silane precursors, after which the hydrolyzed 3F and *n*PM solutions were diluted in DDI H_2O followed by dropwise addition of NH_4OH to induce condensation and generate the nanoparticles.

20 mL glass scintillation vials at 23 °C. Due to their high hydrophobicity indices, the 3F ($\rho > 1$) drops to the bottom and *n*PM ($\rho < 1$) disperse at the top of the water, forming lenses of an immiscible precursor. Under these conditions, 3F hydrolysis was slower (10 h) than *n*PM (6 h). 3F and *n*PM hydrolyses (solubilization) were confirmed by the absence of the precursor lenses. Three different concentrations of 3F and *n*PM (0.008, 0.01, and 0.04 M) were prepared in separate 20 mL glass vials and 0.05 M NH_4OH was added with stirring to generate NPs with different sizes. A schematic for the experimental steps is shown in Figure 1.

Hydrodynamic sizes of the NPs were monitored by dynamic light scattering (DLS) every 15 min from 50 μL aliquots. Once consecutive DLS measurements reported NPs had stopped growing, the reactions were stopped by centrifuging the solutions at 14 000 rpm for 30 min to pellet the NPs, followed by rinsing with DDI H_2O. In contrast to the hydrolysis rates, the condensation of 3F in the basic aqueous solution was faster than *n*PM. Prior to centrifuging the NP-containing solutions, 0.5 mL aliquots were separated from each reaction vessel and stored in 1.5 mL vials prior to drop-casting on freshly cleaved mica for atomic force microscopy (AFM) analysis.

Tuning silica NPs to smaller sizes by reducing the concentration of the silane precursor with respect to a basic catalyst is a common approach, but has practical limitations due to increased synthesis times and decreased yields. In our study, concentrations <0.008 M of 3F and *n*PM failed to yield nanoparticles within the reaction window of 24 h based on visual turbidity and DLS analyses (data not shown). Pelleted NPs were separated from the supernatant, which would contain any unreacted, hydrolyzed silanes. Pellets were then washed with DDI water and repelleted before they were freeze-dried overnight using a Labconco FreeZone Freeze Dry System (Labconco Corporation, Kansas City, MO).

These dried NPs were analyzed for their hydrophobicity, chemical composition, and crystallinity using water contact angle, attenuated total reflection-Fourier transform infrared (ATR-FTIR), and X-ray diffraction (XRD), respectively. As a comparison for XRD, TEOS-based SiO_2 NPs were synthesized through the traditional Stöber method. Briefly, 0.2 mL (90 mM) of TEOS was added in 10 mL of water−ethanol (1:1) solution. Then, 0.1 mL (12 mM) of NaOH was added dropwise to generate silica colloidal particles. To understand the mechanism of hydrophobic nanoparticle assembly from a single-precursor silane, di-alkoxysilane (D3F) was also studied under similar reaction conditions to 3F and *n*PM.

Dynamic Light Scattering and ζ-Potential Analysis. NP hydrodynamic size distributions were measured using DLS (DynaPro NanoStar, Wyatt Technology Corporation, Santa Barbara, CA), with a 658 nm laser. Measurements were taken on the washed and resuspended NPs using a disposable cuvette filled with 50 μL aliquots containing the NPs. The intensity autocorrelation function was converted to a hydrodynamic radius based on the Stokes−Einstein equation using a regularization fitting method employed in the Dynamics software (version 7.0.3, Wyatt Technology Corporation, Santa Barbara, CA). NP surface charge was measured in a disposable cuvette using a Brookhaven ZetaPlus ζ-potential analyzer (Holtzville, NY) in 1.5 mL of a 1 mM KCl electrolyte solution. For both DLS and ζ-potential, 10 acquisitions were collected for each measurement, using three replicate samples per NP. Statistics for particle size and surface charge were performed using one-way analysis of variance (ANOVA) with SAS Studio software and $\alpha < 0.05$.

Atomic Force Microscopy. AFM images were acquired using a Nanoscope III Bioscope (Digital Instruments, Inc.) in tapping mode at ambient conditions at a scan rate of 256 Hz and scan sizes of 1 μm × 1 μm to 5 μm × 5 μm. NP solutions were drop-cast on freshly cleaved mica, then gently washed with DDI water and air-dried before imaging. Budget sensor aluminum-coated AFM tips were obtained from TED Pella Inc., CA (BS TAP300AL-G-50). NP sizes were individually measured on 5 μm × 5 μm images using the line-cut analysis function of the Nanoscope software (v5.12). The polydispersity was assessed from histograms constructed from 10 measurements of particle sizes over 10 images. All presented images were collected using the same AFM tip to better control for tip effects.

Scanning Electron Microscopy (SEM) with Energy-Dispersive Spectroscopy (EDS). NP morphology and elemental composition were determined by SEM (FEI Quanta FEG 650) with EDS using an X-Max detector (Oxford Instruments). NP solutions were drop-cast onto copper tape mounted on aluminum sample stubs and allowed to air-dry before drying under vacuum. The atomic weight percentages of Si, O, C, and F were determined for scans over particle assemblies to reduce contributions from the Cu tape. Elemental distribution on 3F and *n*PM was visualized through false coloring using Oxford Aztec Software.

Sessile and Sliding Water Droplet Contact Angles. The hydrophobicity of the samples was measured with a VCA optima digital contact angle instrument (AST Products, Billerica, MA). A 6 μL droplet of DDI water was deposited on NP thin films prepared on double-sided tape over glass slides. Thin films were prepared by dusting NP powders on double-sided tape affixed to glass slides. The glass slides were gently shaken to remove excess NP powder leaving a thin NP layer on the tape. These NP thin films are shown in Figure S1. The static water contact angle was measured for three drops per surface. Sliding angle videos were taken at 120 frames per second using an iPhone 6s. A second glass slide was used as a wedge to tilt the NP-coated slide (<5°). Tilt angles were measured using the protractor tool in Image-J. Tilt angles were varied to identify the difference in sliding angle between the 3F and *n*PM NP-coated surfaces.

Powder X-ray Diffraction. The fluorinated and alkylated NP powders were manually compacted into metal sample holders to form a smooth, flat surface for analysis. Samples were analyzed using a

https://doi.org/10.1021/acsanm.1c00398
ACS Appl. Nano Mater. 2021, 4, 4092−4102

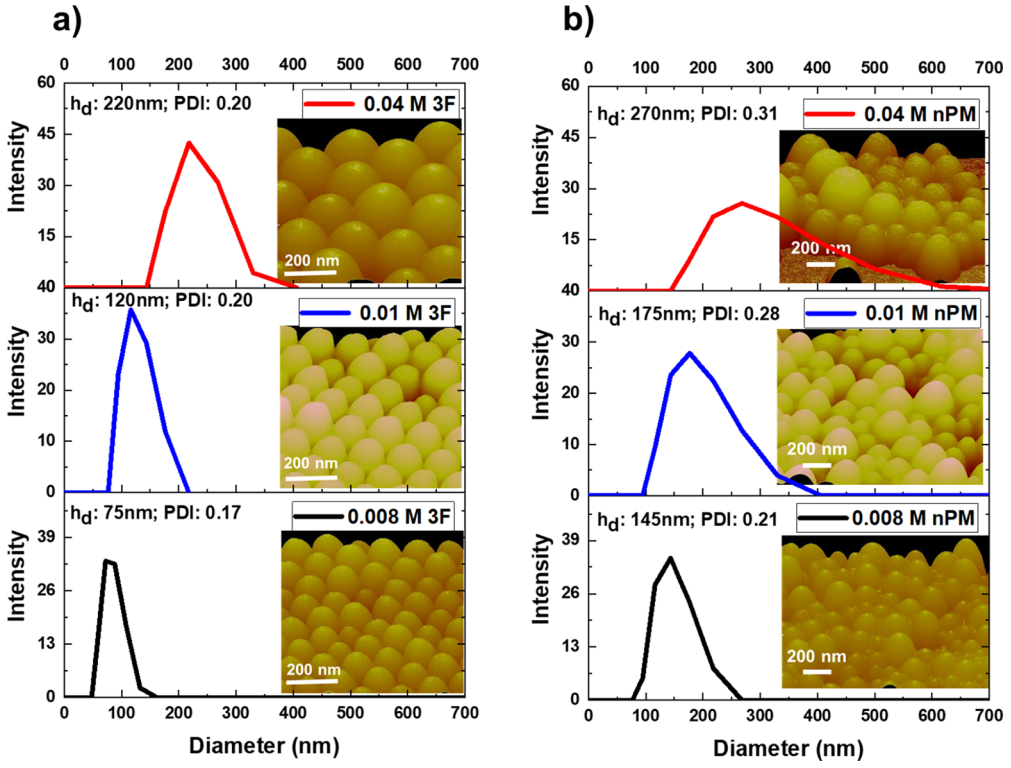

Figure 2. Hydrodynamic diameter of (a) fluoro-silica NPs and (b) alkyl-silica NPs generated from 0.008, 0.01, and 0.04 M of 3F and *n*PM, respectively. The insets show the AFM images, hydrodynamic diameters (h_d), and polydispersity indices (PDI) of the corresponding NPs.

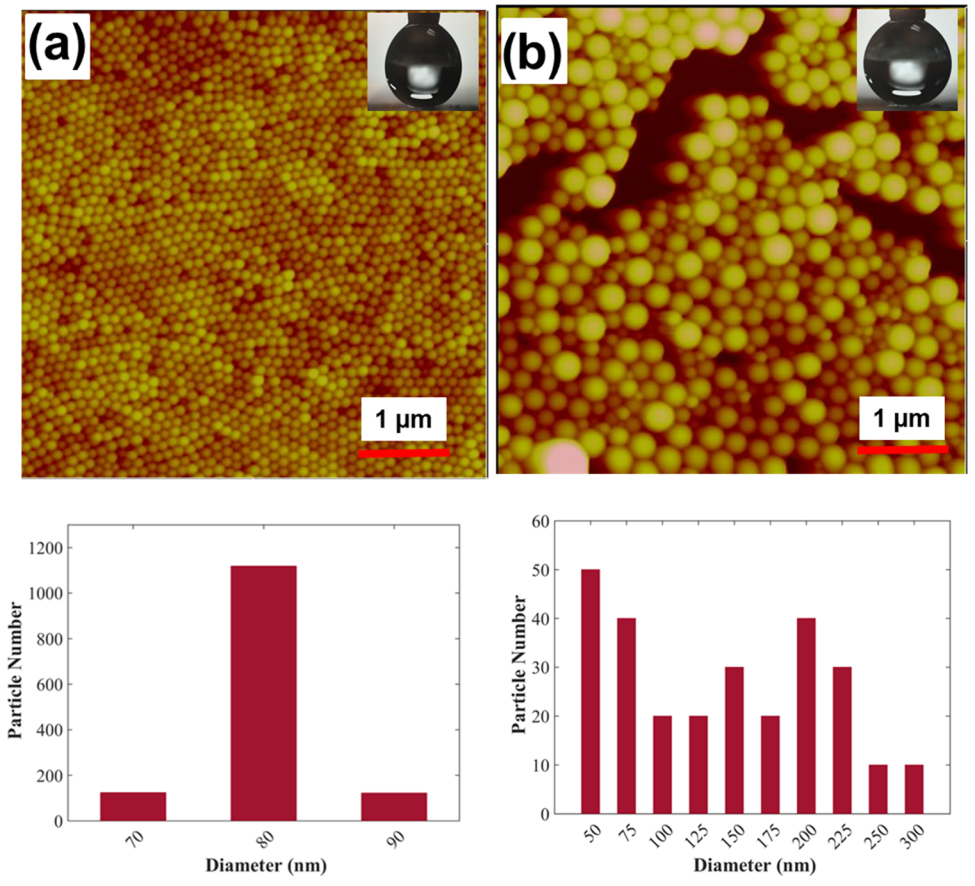

Figure 3. AFM images of (a) fluorinated NPs and (b) alkylated NPs generated from 0.008 M 3F and *n*PM, respectively. At the bottom, histograms of the diameter of the corresponding nanoparticles are shown. The insets show the sessile water droplet on the NPs-coated surfaces.

https://doi.org/10.1021/acsanm.1c00398
ACS Appl. Nano Mater. 2021, 4, 4092−4102

Panalytical X'Pert Pro X-ray Diffraction Spectrometer (PW3373/00 Cu LFF DK194241 X-ray) under 45 kV tension and 40 mA current operating conditions. Diffraction patterns were measured from 2θ of 2 to 75°. The peaks and profiles of the diffraction patterns were interpreted using the X'Pert High Score software program.

Fourier Transform Infrared Spectroscopy. The ATR-FTIR spectra of lyophilized silica NPs were collected using a Varian 660-IR with a horizontal single reflection Pike Technologies MIRacle attenuated total reflectance (ATR) unit, fitted with a ZnSe crystal. Readings were taken after averaging 20 scans over the range of 600–2000 cm^{-1} with a resolution of 1 cm^{-1}. Prior to each reading, a background scan was acquired.

RESULTS AND DISCUSSION

Under the aqueous, weak acid/base catalysis conditions employed here, a visible condensate could be used to monitor reaction progression, supported by DLS. As hydrolyzed silane concentrations were decreased (0.04, 0.01, 0.008 M), turbidity was less evident and the presence of NPs in these solutions was confirmed with DLS, as shown in Figure 2. The 3F and *n*PM particle sizes decreased as silane concentrations were decreased as observed in the DLS size histograms. Additionally, for each of the investigated hydrolyzed silane concentration (0.04, 0.01, 0.008 M), the final particle size and polydispersity indices (PDI) were always lower for 3F than for *n*PM. The average hydrodynamic diameters of the 3F particles were 220 nm (0.04 M), 120 nm (0.01 M), and 75 nm (0.008 M), as shown in Figure 2a. For the same concentrations of hydrolyzed precursor, the average hydrodynamic diameters (h_d) of the alkylated NPs were 270, 175, and 145 nm, respectively, as shown in Figure 2b.

AFM was used as a complementary size analysis technique to DLS to provide particle morphology and surface roughness details. The AFM images in Figure 2 support the DLS PDI trends, revealing more monodisperse 3F NPs than *n*PM NPs for all three precursor silane concentrations. A broader distribution of *n*PM NP sizes is observed by AFM, reflecting the higher PDI values obtained for *n*PM NP solutions by DLS. Highly spherical particles are observed for both 3F and *n*PM. Additional size and polydispersity analyses are presented in Figure 3 for the smallest attainable NPs synthesized from 0.008 M 3F and *n*PM. The fluorinated NPs in Figure 3a exhibit long-range ordering, forming arrays of close-packed sub-100 nm spherical particles, with most of the 3F NPs having diameters near 80 nm as seen in the corresponding size histogram. The alkylated *n*PM NPs in Figure 3b were significantly more polydisperse, varying in size from 50 to 300 nm.

The smaller particle sizes and lower PDI values of 3F compared to *n*PM are attributed to the differences in reaction rates between these silanes to form the initial nucleus, or seed particles, and subsequent assembly into larger particles.[50−52] The highly electronegative fluorines in 3F are just three carbons removed from the Si atom, generating a greater partial positive charge on Si than for the nonfluorinated *n*PM. The trifluoropropyl moiety also exhibits greater steric constraints than the *n*-propyl moiety of *n*PM. We have previously reported on how these differences in side-group hydrophobicity, electronegativity, and steric bulk influenced the sol−gel kinetics for an unstirred aqueous reaction system.[53] These differences in reaction kinetics arising from silane precursor properties are considered the dominating factors in controlling the size and shape of the particles generated during the condensation process—in particular, the steric hindrance associated with the bulky CF_3 side chain of 3F is expected to result in a slower condensation process compared to *n*PM, which may favor the formation of more nuclei and smaller overall particles.

The water contact angles obtained on these NP films were 170° for 3F and 165° for *n*PM, as shown in the insets in Figure 3a,b, with angle measurements presented in Figure S2. The superhydrophobic behaviors of these NPs were further evaluated through sliding angles, provided in the videos in the Supporting Information (Videos SMV1 and SMV2). The superhydrophobic character of both the fluorinated NPs (Video SMV1) and alkylated NPs (Video SMV2) is demonstrated by water sliding angles of ∼0 and ∼4°, for 3F and *n*PM, respectively. Single frames from these videos are shown in Figure S3. The water contact angles >165° and sliding angles <5° classify both 3F and *n*PM as superhydrophobic silica NPs.

To assess the crystal structures of the fluorinated 3F and alkylated *n*PM silica NPs, XRD was performed (Figure 4). The

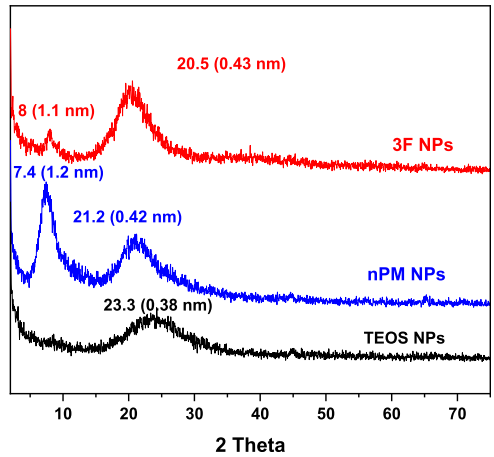

Figure 4. XRD patterns of the fluorinated/3F-based NPs (top), alkylated/*n*PM-based NPs (middle), and TEOS-based silica NPs (bottom). The peak 2θ values and the calculated Bragg *d*-spacings are indicated next to each peak.

fluorinated NPs showed a sharp peak at 2θ = 8° and a wider peak at 20.5°, which were also present for alkylated NPs but shifted to 7.4 and 21.2°, respectively. These two diffraction peaks are attributed to cage/cube structures in the macromolecular network of oligomeric silsesquioxanes, POSS, which are known to form as trifunctional silane condense.[54−56] For POSS particles, peaks at 2θ < 10° are proposed to correspond to the intermolecular spacing of the fourfold siloxane rings present in a cage/cubelike silsesquioxane structural unit in the matrix.[54−56] The 2θ < 10° peaks also are influenced by the distance between the oxygens of adjacent molecules that are separated by Si with a pendant organic group.[57] The 2θ peaks near 20° typically represent the Si−O structure, with peak positions reflecting spacing between silicon atoms connected by an oxygen bridge in the amorphous silica structure.[54,55,58] Unlike the trialkoxysilane (3F/*n*PM)-based NPs prepared here, typical silica NPs synthesized from tetra-alkoxysilane (TEOS) only have a single 2θ peak near 23° representing their amorphous nature,[59] as seen in the XRD pattern for TEOS NPs also shown in Figure 4.

The calculated Bragg *d*-spacings for the 3F, *n*PM, and TEOS 2θ peaks are included next to each diffraction peak in Figure 4. Constraints on the Si−O−Si bonds for the semicrystalline 3F and *n*PM particles compared to the amorphous TEOS particles

https://doi.org/10.1021/acsanm.1c00398
ACS Appl. Nano Mater. 2021, 4, 4092−4102

are evident in the *d*-spacing increase from 0.38 nm for TEOS to 0.42 and 0.43 nm for *n*PM and 3F particles, respectively. For the $2\theta < 10°$ peaks, the d-spacing for 3F is 1.1 nm compared to 1.2 nm for *n*PM. The apparent larger Si−O−Si spacing at $2\theta > 20°$ and smaller length of the intermolecular spacing ($2\theta < 10°$) in the fluorinated NP structures compared to that of the alkylated NPs is attributed to differential steric and inductive effects of the trifluoropropyl group in 3F vs the *n*-propyl group in *n*PM molecules. Rios et al. observed a similar trend in the backbone and intermolecular chain spacing among ethyl-trialkoxysilane and methyl-trialkoxysilane, where they reported that *d*-spacing was larger at 2θ near 20° and smaller at $2\theta < 10°$ in the ethyl-trialkoxysilane compared to the methyl-trialkoxysilane.[54,60] The induced partial charge on the silicon atoms is higher in the fluorinated NPs compared to the alkylated NPs due to the electron-withdrawing fluorine functionality, which results in an increase in the bond distance between silicon atoms connected by oxygen (Si−O−Si). The shorter distance between intermolecular spacing in the fluorinated NPs compare to alkylated NPs could be due to the difference in the orientation of the cage structures. The higher peak intensity at $2\theta < 10°$ and lower peak intensity at $2\theta > 20°$ in the XRD spectra of the alkylated NPs support the formation of more semicrystalline cage structures in the alkylated NPs compared to the fluorinated NPs. These data suggest that the cage-type structures pack more efficiently than the network structures. Cage-type formation during *n*PM and 3F condensation processes would explain the XRD peaks for these two SHS NPs, which are absent in the TEOS NPs. As both *n*PM and 3F precursors have three reactive methoxy groups, unsatisfied bonding is possible during the condensation process, leaving exposed silanol groups. As the trifluoropropyl moiety also exhibits greater steric constraints than the *n*-propyl moiety of *n*PM, the potential for unreacted silanols may be greater for 3F than *n*PM.

ATR-FTIR spectra present a better understanding of the structural formation of both fluorinated and alkylated NPs, as shown in Figure 5. The strong bands of the stretching vibration of Si−O−Si between 1210 and 1000 cm^{-1} confirm the SiO_2 polymeric network in all fluorinated, alkylated NPs and TEOS-based NPs.[61−63] The asymmetric stretching vibration of Si−O−Si at 1108 and 1062 cm^{-1} and symmetric stretching vibration at 1015−1025 cm^{-1} in both 3F and *n*PM spectra represent the cage/cubelike structures of POSS generated as hydrolyzed 3F and *n*PM condense to form NPs.[54,64] The asymmetric vibration of Si−O−Si observed at 1108 cm^{-1} is also assigned to a cage structure;[65] thus, the ratio of the peak intensities at 1108 and 1062 cm^{-1} is used to assess the amount of cage/cube structure vs random network structures.[54,64,65] The higher relative intensity of 1062 cm^{-1} vs 1108 cm^{-1} observed in the 3F NP spectrum suggests a more random structure compared to that in the *n*PM NP spectrum. The peaks at 950 and 900 cm^{-1} observed for 3F support the presence of Si−OH[45,66,67] and nonbridging "free" broken Si−O bonds,[62,63,66,68] respectively. The 950 cm^{-1} peak was also observed in TEOS-based NPs, as might be anticipated for a nonfunctionalized "bare" silica NP. For 3F, very minor peaks around 3700−3800 cm^{-1} representing the Si−OH were also discernible. The presence of both Si−OH and free Si−O− structure in the polymeric network further supports the formation of partial/opened POSS cage/cube structures in the fluorinated 3F NPs. Furthermore, the absence of an absorption peak at 950 cm^{-1} possibly indicates the formation of a closed-loop or complete formation of the POSS cage/cube structure in the alkylated NPs. However, a small shoulder at 900 cm^{-1} represents the free broken bonds (Si−O−) as the POSS cages/cubes were restructuring in the alkylated NPs.[66]

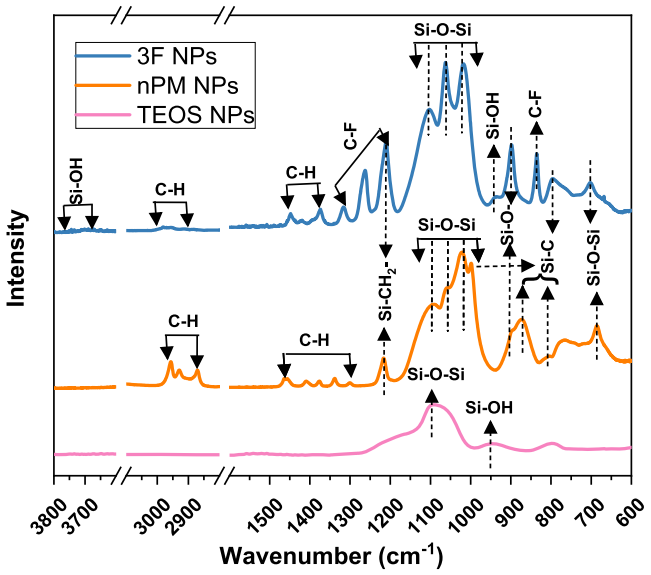

Figure 5. ATR-FTIR spectra of the fluorinated (top), alkylated (middle), and nonfunctionalized (bottom)-based silica NPs from 3F, *n*PM, and TEOS silane precursors.

The presence of the trifluoro functionality in the 3F NPs was confirmed by peaks at 840, 1210, 1260, and 1310 cm^{-1} representing the stretching vibration for C−F.[45,61,69] A peak at 1210 cm^{-1} representing the deformation vibration of Si−CH_2− exists in both particles due to the respective fluoro- and alkyl-propyl functionalities. Thus, the absorption intensity at 1210 cm^{-1} is greater in the fluorinated NP spectrum as it overlaps with the C−F vibration. The deformation vibration of Si−CH_2− can also be seen at 800 cm^{-1} in the spectrum for 3F NPs and at 775, 880, and 995 cm^{-1} for *n*PM NPs.[61,63] Bending and stretching vibrational modes of C−H are observed from 1320 to 1450 and 2850 to 3000 cm^{-1} in both the spectra, reflecting the *n*-propyl functionality in both particles.[63,70]

We further studied the ζ-potential of both the fluorinated and alkylated NPs. At neutral pH, the observed ζ-potentials for fluorinated and alkylated NPs were -23 ± 3 and -33 ± 10 mV, respectively, but showed no statistically significant difference. These values are similar to the reported values for multisilane, multistep ORMOSIL particles.[71] Bare silica NPs, in contrast, yield ζ-potential values closer to −45 mV at pH 7. The presence of Si−OH and Si−O− as observed in the FTIR spectrum of fluorinated but not in alkylated NPs would be expected to yield 3F particles with a more negative ζ-potential than *n*PM NPs. The absence of a statistical difference in 3F and *n*PM particle surface charge as determined through ζ-potential may reflect differences in surface accessibility of the silanol groups, as FTIR is not restricted to surface chemistries. Additional insight into the 3F and *n*PM particle chemical functionalities was obtained through SEM with EDS elemental analysis (Figure S6). The SEM imaging confirmed spherical 3F and *n*PM particles, while EDS revealed alkyl and fluoro surface chemistries with atomic percent ratios supporting the anticipated $SiO_{1.5}$ structure for both 3F and *n*PM.

Based on the XRD, FTIR, and EDS analyses, the anticipated POSS molecular structures generated during the condensation of hydrolyzed 3F and *n*PM are depicted in Figure 6a,b,

https://doi.org/10.1021/acsanm.1c00398
ACS Appl. Nano Mater. 2021, 4, 4092−4102

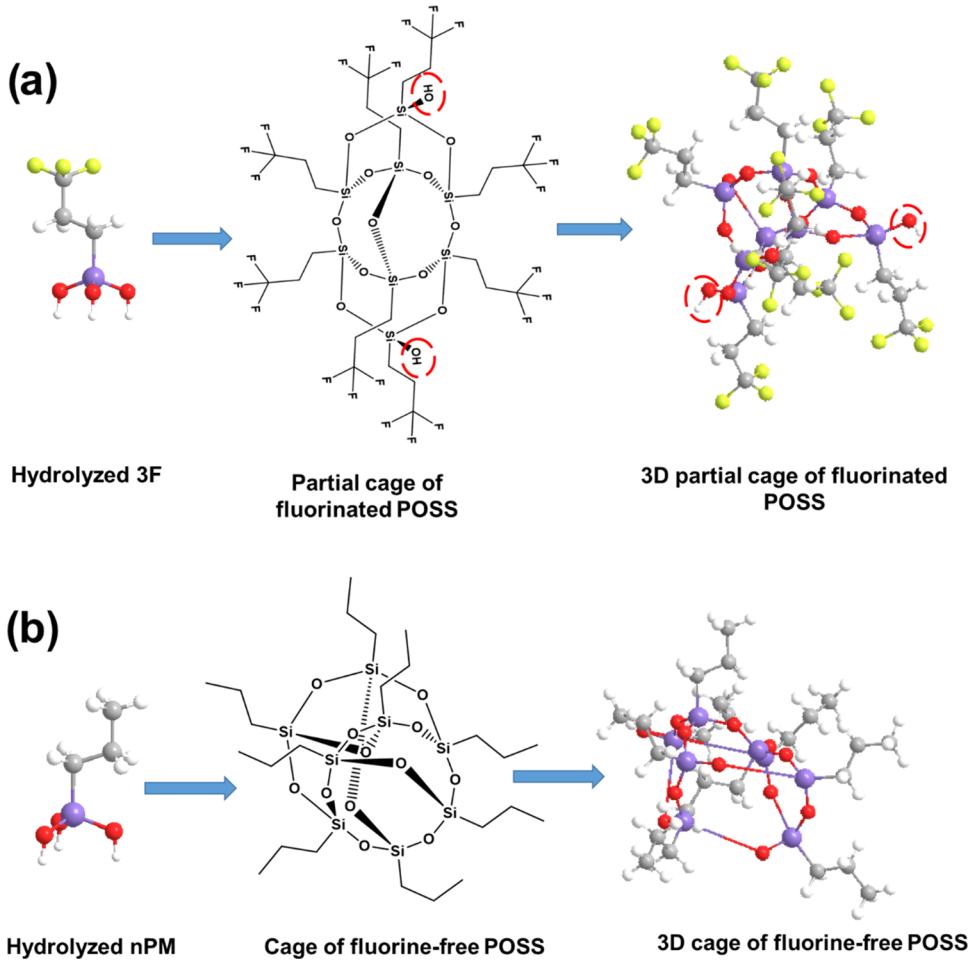

Figure 6. Chemical structures of the (a) partial cage of fluorinated POSS and (b) cage of alkylated POSS. (Chemical structures are drawn and modeled using ChemDraw 16.0).

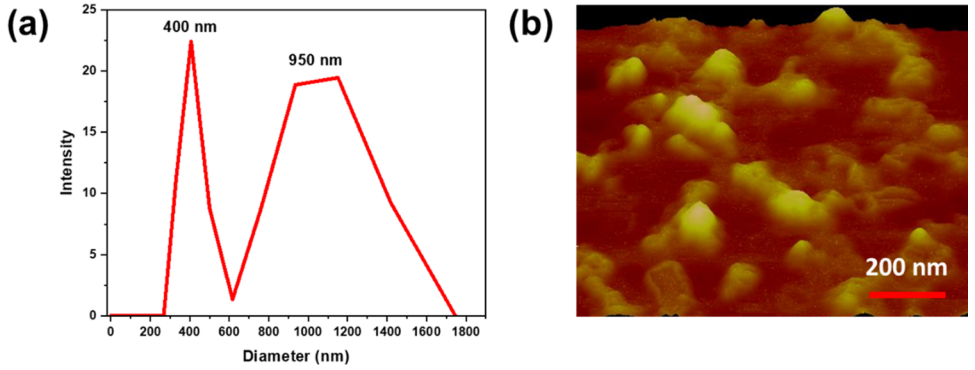

Figure 7. (a) Hydrodynamic sizes of the particulate generated from the condensation of D3F; (b) AFM image of the particulates generated from D3F.

respectively. Figure 6a shows the partially open cage/cube structures of the tri-fluoro-*n*-propyl POSS with the unbridged Si−OH groups circled. In contrast, a closed cage structure is depicted for the nonfluorinated analog, *n*-propyl POSS (Figure 6b). These POSS cages may act as the basic units for the development of the seed particles, which subsequently assemble to form mature NPs as the sol−gel reaction progresses. The open and closed cage structures of the fluorinated and alkylated POSS units, respectively, may also contribute to the differences in fluoro- and alkyl-NP sizes and polydispersity as observed in the DLS and AFM analyses.

The tri-alkoxy functionality around the Si atom in 3F and *n*PM allows for the formation of three-dimensional (3D) structures such as the POSS units and higher-ordered structures through branching and network polymerization. Physical cross-linking is also possible through van der Waals forces and hydrophobic interactions. To identify whether physical interactions alone can promote the assembly and stability of these silanes, a di-alkoxy analog of 3F, referred to as D3F was employed. Unlike the trialkoxysilanes, D3F has only two hydrolyzable alkoxy functionalities and thus can only form a linear siloxane backbone, which through intra- and interchain

https://doi.org/10.1021/acsanm.1c00398
ACS Appl. Nano Mater. 2021, 4, 4092−4102

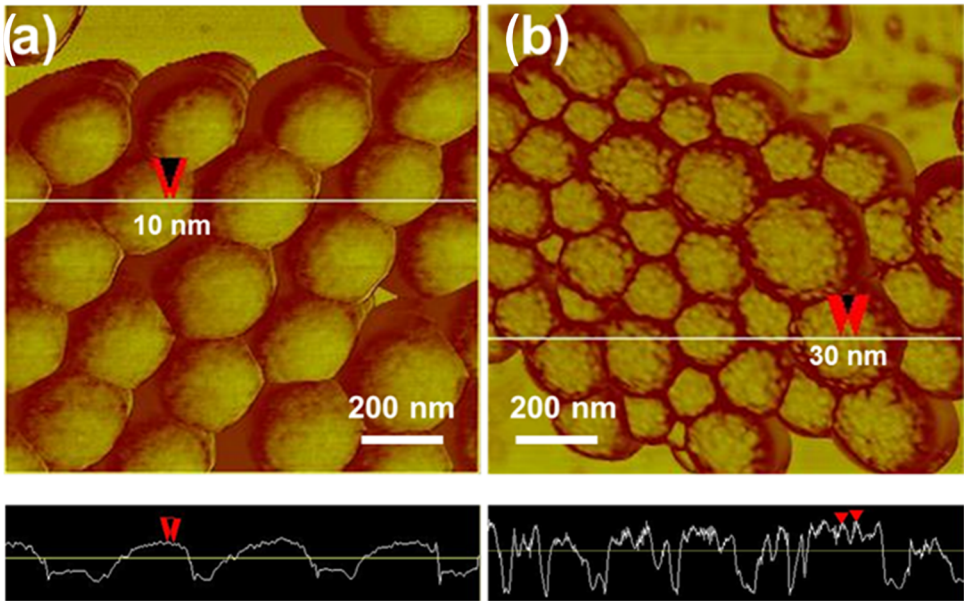

Figure 8. AFM phase images of (a) fluorinated and (b) alkylated NPs generated from 0.04 M 3F (a) and *n*PM (b). Representative line-cut profiles are presented below each image, where the *y*-axis represents differences in compliance as the tip resonates across the "hard" and "soft" regions of the NPs.

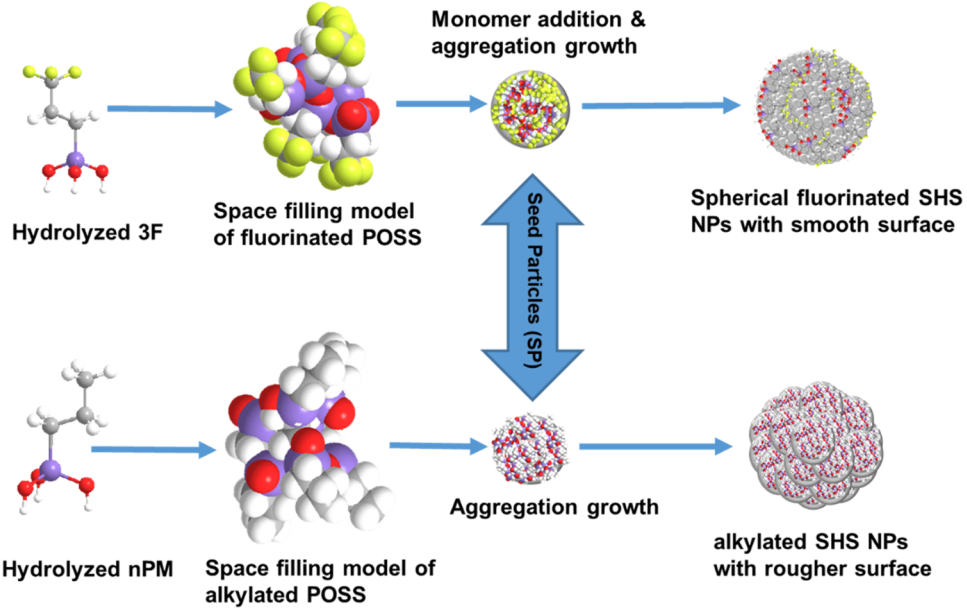

Figure 9. Schematic presentation of polymerization proposed route to form the fluorinated (top) and alkylated (bottom) SHS NPs. (Chemical structures are drawn and modeled using ChemDraw 16.0).

physical interactions may assemble to form particles. The D3F sol–gel process resulted in a cloudy precipitate that upon purification did not indicate the formation of distinct NPs. The DLS hydrodynamic sizes were bimodal, with peaks at 400 and 950 nm, as shown in Figure 7a. The 950 nm diameter peak is very broad and may represent aggregates of the more defined particles contributing to the narrower 400 nm diameter peak.

SHS Silica NP Formation Mechanism. The assembly mechanisms of the fluorinated and alkylated NPs were further investigated using AFM phase imaging, which is more sensitive to heterogeneity in material compliance that does not show up in the topography images. Representative images of the fluorinated and alkylated NPs are presented in Figure 8 along with cross-sectional line profiles. This analysis of fluorinated NPs reveals a relatively smooth surface with a faint dimpling pattern with a periodicity of ~10 nm (Figure 8a). For the alkylated NPs, a much more pronounced surface patterning is observed, with a periodicity of ~30 nm (Figure 8b). Additional AFM topography and phase images are shown in Figures S4 and S5.

The apparent differences between the fluorinated and alkylated NP morphologies suggest that they form through two distinct growth models, namely: (i) monomer addition model and (ii) aggregation growth model.[51,52] The monomer addition model describes the initial formation of silica nuclei, or seeds, after which it grows further with the addition of silanol monomers, maintaining the monodispersity throughout the whole process. In the aggregation growth model, the initially formed seed particles aggregate and subsequently grow into

https://doi.org/10.1021/acsanm.1c00398
ACS Appl. Nano Mater. 2021, 4, 4092–4102

larger particles with the attachment of silanol monomers or oligomers, which trends toward a more polydisperse size distribution. Based on the structural and morphological analysis, it appears that the alkylated NPs formed following an aggregation growth model generate the larger-sized particles. However, the smoother surfaces of the fluorinated NPs suggest a mixture of the aggregation growth model and the monomer addition model. Both growth models are schematically depicted in Figure 9. The initially formed seed particles from the 3F precursor contain hydroxyl functionality, which may allow these seed particles to grow both with the addition of hydrolyzed monomers and aggregation with other seeds. Depending on the reaction conditions, the size of the particles varies as reported for Stöber syntheses. The reaction condition influence on particle size is well-known.

For our POSS-type ring structure, we can only assume that these are the fundamental assembly units for what we term "seed" particles that further assemble to form "mature" NPs. The presence of unreacted Si−OH groups on particle surfaces may lead to water adsorption that could lead to a loss of hydrophobicity with time. After 1 year of storage as dry powders, surface stability was tested by dispersing particles in DDI H_2O with 30 min of bath sonication (shown in Figure S7). Following this treatment, the particles remained immiscible, immediately partitioning to the air/water interface, demonstrating the longevity of the superhydrophobic properties. These outcomes support applications of the fluoro- and alkyl-silane NPs requiring durable superhydrophobicity.

CONCLUSIONS

The aqueous "green" synthesis presented here can be used to tune superhydrophobic NP size through silane precursor concentration with a practical lower particle size limit near 50 nm. Fluorinated and alkylated silica NPs of 50−300 nm were successfully synthesized in the aqueous solution from 3,3,3-propyl(trifluoro)trimethoxysilane (3F) and *n*-propyltrimethoxysilane (*n*PM) single-source precursors, respectively, without salts or surfactant templates. Water contact angles >160° and sliding angles <5° measured for surfaces coated with these NPs confirmed superhydrophobicity. AFM topography and phase imaging revealed 3F NPs were smoother, smaller, and more monodisperse than the corresponding *n*PM NPs. XRD and ATR-FTIR spectra support the formation of POSS cages for *n*PM, and partial cage structures for 3F. Moderate negative ζ-potentials for both NP types suggest the presence of free surface silanols on the particles; however, the POSS assembly to form seed particles that assemble/grow into mature NPs may follow distinct pathways for 3F and *n*PM based on AFM phase imaging, which revealed dimpled surfaces for *n*PM particles compared to smooth surfaces for 3F. Based on these analyses, 3F NPs may form through an aggregation and monomer addition growth model, whereas *n*PM NPs appear to follow an aggregation growth model. The network polymerization of both silanes to form NPs is supported by the absence of spherical NP formation by a di-alkoxy analog of 3F. Superhydrophobic silica NP synthesis from a single-precursor silane eliminates the postsynthesis capping steps required in conventional methods and guarantees that each Si atom is "fully functionalized" with the selected hydrophobic moiety. Limitations in this technique will arise from side-chain length/bulk that may restrict chain assembly (folding) and cross-linking, likely leading to a greater number of unreacted silanols. The surface accessibility of the hydrophobic groups as well as unreacted silanols was interrogated with static and sliding water contact angles, which demonstrated that 3F particle films were slightly more hydrophobic than *n*PM films even though FTIR and XRD supported greater free silanols on the 3F particles. For applications where fluorine chemistry is undesirable, such as with toxicity concerns, the alkyl-silane synthesis route yielded similar water contact and sliding angles, but yield NPs of greater size and polydispersity than the fluorinated counterparts. The cost of the alkyl-silane is significantly less than the fluoro-silane, which may also favor its selection for SHS NP synthesis for surface coating applications.

ASSOCIATED CONTENT

Supporting Information

The Supporting Information is available free of charge at https://pubs.acs.org/doi/10.1021/acsanm.1c00398.

Video SMV1 (MOV)

Video SMV2 (MOV)

Superhydrophobic thin films prepared from 3F and *n*PM NP; sessile water drop contact angles on *n*PM and 3F NP-coated glass; water sliding angles on *n*PM and 3F NP-coated glass; AFM topography images of fluorinated and alkylated NPs; AFM topography, amplitude, and phase images of fluorinated and alkylated NPs; SEM images with EDX analysis of 3F and *n*PM particles; and nondispersible NPs in water after 1 year (PDF)

AUTHOR INFORMATION

Corresponding Author

David W. Britt − *Department of Biological Engineering, Utah State University, Logan, Utah 84322-4105, United States;* orcid.org/0000-0002-9753-6404; Email: david.britt@usu.edu

Authors

Abul Bashar Mohammad Giasuddin − *Department of Biological Engineering, Utah State University, Logan, Utah 84322-4105, United States;* orcid.org/0000-0003-2236-799X

Anthony Cartwright − *Department of Biological Engineering, Utah State University, Logan, Utah 84322-4105, United States*

Complete contact information is available at: https://pubs.acs.org/10.1021/acsanm.1c00398

Notes

The authors declare no competing financial interest.

ACKNOWLEDGMENTS

The authors gratefully acknowledge funding from the USU AES Station, Project 1280 (A.B.M.G.); AFRI USDA-NIFA 2016-08771 and NSF CBET 1705874 (D.W.B. and A.C.); and the USU RGS Presidential Doctoral Research Fellowship (A.C.). USU Core Microscopy Facility and SEM instrumentation support was from NSF CMMI 1337932.

REFERENCES

(1) Bitar, A.; Ahmad, N. M.; Fessi, H.; Elaissari, A. Silica-Based Nanoparticles for Biomedical Applications. *Drug Discovery Today* **2012**, *17*, 1147−1154.

(2) Tang, F.; Li, L.; Chen, D. Mesoporous Silica Nanoparticles: Synthesis, Biocompatibility and Drug Delivery. *Adv. Mater.* **2012**, *24*, 1504−1534.
(3) Kasaai, M. R. Nanosized Particles of Silica and Its Derivatives for Applications in Various Branches of Food and Nutrition Sectors. *J. Nanotechnol.* **2015**, *2015*, No. 852394.
(4) Chang, H.; Sun, S.-Q. Silicon Nanoparticles: Preparation, Properties, and Applications. *Chin. Phys. B* **2014**, *23*, No. 088102.
(5) Tang, D.; Zhang, W.; Qiao, Z.; Liu, Y.; Huo, Q. Functionalized Mesoporous Silica Nanoparticles as a Catalyst to Synthesize a Luminescent Polymer/Silica Nanocomposite. *RSC Adv.* **2016**, *6*, 16461−16466.
(6) Chan, C.; Sepunaru, L.; Sokolov, S. V.; Kätelhön, E.; Young, N. P.; Compton, R. G. Catalytic Activity of Catalase−Silica Nanoparticle Hybrids: From Ensemble to Individual Entity Activity. *Chem. Sci.* **2017**, *8*, 2303−2308.
(7) Popova, M.; Ristić, A.; Lazar, K.; Maučec, D.; Vassileva, M.; Tušar, N. N. Iron-Functionalized Silica Nanoparticles as a Highly Efficient Adsorbent and Catalyst for Toluene Oxidation in the Gas Phase. *ChemCatChem* **2013**, *5*, 986−993.
(8) Hyde, E. D. E. R.; Seyfaee, A.; Neville, F.; Moreno-Atanasio, R. Colloidal Silica Particle Synthesis and Future Industrial Manufacturing Pathways: A Review. *Ind. Eng. Chem. Res.* **2016**, *55*, 8891−8913.
(9) Stöber, W.; Fink, A.; Bohn, E. Controlled Growth of Monodisperse Silica Spheres in the Micron Size Range. *J. Colloid Interface Sci.* **1968**, *26*, 62−69.
(10) Rao, K. S.; El-Hami, K.; Kodaki, T.; Matsushige, K.; Makino, K. A Novel Method for Synthesis of Silica Nanoparticles. *J. Colloid Interface Sci.* **2005**, *289*, 125−131.
(11) Hartlen, K. D.; Athanasopoulos, A. P. T.; Kitaev, V. Facile Preparation of Highly Monodisperse Small Silica Spheres (15 to >200 Nm) Suitable for Colloidal Templating and Formation of Ordered Arrays. *Langmuir* **2008**, *24*, 1714−1720.
(12) Dixit, C. K.; Bhakta, S.; Kumar, A.; Suib, S. L.; Rusling, J. F. Fast Nucleation for Silica Nanoparticle Synthesis Using a Sol−Gel Method. *Nanoscale* **2016**, *8*, 19662−19667.
(13) Bhakta, S.; Dixit, C. K.; Bist, I.; Jalil, K. A.; Suib, S. L.; Rusling, J. F. Sodium Hydroxide Catalyzed Monodispersed High Surface Area Silica Nanoparticles. *Mater. Res. Express* **2016**, *3*, No. 075025.
(14) Rahman, I. A.; Jafarzadeh, M.; Sipaut, C. S. Synthesis of Organo-Functionalized Nanosilica via a Co-Condensation Modification Using γ-Aminopropyltriethoxysilane (APTES). *Ceram. Int.* **2009**, *35*, 1883−1888.
(15) Liberman, A.; Mendez, N.; Trogler, W. C.; Kummel, A. C. Synthesis and Surface Functionalization of Silica Nanoparticles for Nanomedicine. *Surf. Sci. Rep.* **2014**, *69*, 132−158.
(16) Dixit, C. K.; Bhakta, S.; Macharia, J.; Furtado, J.; Suib, S. L.; Rusling, J. F. Novel Epoxy-Silica Nanoparticles to Develop Non-Enzymatic Colorimetric Probe for Analytical Immuno/Bioassays. *Anal. Chim. Acta* **2018**, *1028*, 77−85.
(17) Xu, L.; Karunakaran, R. G.; Guo, J.; Yang, S. Transparent, Superhydrophobic Surfaces from One-Step Spin Coating of Hydrophobic Nanoparticles. *ACS Appl. Mater. Interfaces* **2012**, *4*, 1118−1125.
(18) Yazdanshenas, M. E.; Shateri-Khalilabad, M. One-Step Synthesis of Superhydrophobic Coating on Cotton Fabric by Ultrasound Irradiation. *Ind. Eng. Chem. Res.* **2013**, *52*, 12846−12854.
(19) Ye, Y.; Zhang, C.; Tian, M.; Du, Z.; Mi, J. Macroscopic and Microscopic Analyses of Hydrophobic Modification of Rubbers with Silica Nanoparticles. *J. Phys. Chem. C* **2015**, *119*, 20957−20966.
(20) Li, X.; Yu, X.; Cheng, C.; Deng, L.; Wang, M.; Wang, X. Electrospun Superhydrophobic Organic/Inorganic Composite Nanofibrous Membranes for Membrane Distillation. *ACS Appl. Mater. Interfaces* **2015**, *7*, 21919−21930.
(21) Sheng, J.; Xu, Y.; Yu, J.; Ding, B. Robust Fluorine-Free Superhydrophobic Amino-Silicone Oil/SiO2Modification of Electrospun Polyacrylonitrile Membranes for Waterproof-Breathable Application. *ACS Appl. Mater. Interfaces* **2017**, *9*, 15139−15147.
(22) Zhou, H.; Wang, H.; Niu, H.; Gestos, A.; Wang, X.; Lin, T. Fluoroalkyl Silane Modified Silicone Rubber/Nanoparticle Composite: A Super Durable, Robust Superhydrophobic Fabric Coating. *Adv. Mater.* **2012**, *24*, 2409−2412.
(23) Li, X.-M.; Reinhoudt, D.; Crego-Calama, M. What Do We Need for a Superhydrophobic Surface? A Review on the Recent Progress in the Preparation of Superhydrophobic Surfaces. *Chem. Soc. Rev.* **2007**, *36*, 1350.
(24) Ngo, C. V.; Chun, D. M. Laser Printing of Superhydrophobic Patterns from Mixtures of Hydrophobic Silica Nanoparticles and Toner Powder. *Sci. Rep.* **2016**, *6*, No. 36735.
(25) Sriramulu, D.; Reed, E. L.; Annamalai, M. Synthesis and Characterization of NIR-Reflective Silica Nanoparticles. *Sci. Rep.* **2016**, *6*, No. 35993.
(26) Guo, F.; Wen, Q.; Peng, Y.; Guo, Z. Fabric and the Application in Oil/Water Separation. *J. Mater. Chem. A* **2017**, *5*, 21866−21874.
(27) Wang, N.; Xiong, D.; Deng, Y.; Shi, Y.; Wang, K. Mechanically Robust Superhydrophobic Steel Surface with Anti-Icing, UV-Durability, and Corrosion Resistance Properties. *ACS Appl. Mater. Interfaces* **2015**, *7*, 6260−6272.
(28) Shang, Q.; Zhou, Y. Fabrication of Transparent Superhydrophobic Porous Silica Coating for Self-Cleaning and Anti-Fogging. *Ceram. Int.* **2016**, *42*, 8706−8712.
(29) Cao, L.; Jones, A. K.; Sikka, V. K.; Wu, J.; Gao, D. Anti-Icing Superhydrophobic Coatings. *Langmuir* **2009**, *25*, 12444−12448.
(30) Zhang, S.; Ouyang, X.; Li, J.; Gao, S.; Han, S.; Liu, L.; Wei, H. Underwater Drag-Reducing Effect of Superhydrophobic Submarine Model. *Langmuir* **2015**, *31*, 587−593.
(31) Banerjee, I.; Pangule, R. C.; Kane, R. S. Antifouling Coatings: Recent Developments in the Design of Surfaces That Prevent Fouling by Proteins, Bacteria, and Marine Organisms. *Adv. Mater.* **2011**, *23*, 690−718.
(32) Yohe, S. T.; Colson, Y. L.; Grinstaff, M. W. Superhydrophobic Materials for Tunable Drug Release: Using Displacement of Air to Control Delivery Rates. *J. Am. Chem. Soc.* **2012**, *134*, 2016−2019.
(33) Xu, Z.; Zhao, Y.; Wang, H.; Zhou, H.; Qin, C.; Wang, X.; Lin, T. Fluorine-Free Superhydrophobic Coatings with PH-Induced Wettability Transition for Controllable Oil-Water Separation. *ACS Appl. Mater. Interfaces* **2016**, *8*, 5661−5667.
(34) Li, J.; Zhou, L.; Yang, N.; Gao, C.; Zheng, Y. Robust Superhydrophobic Coatings with Micro- and Nano-Composite Morphology. *RSC Adv.* **2017**, *7*, 44234−44238.
(35) Shieh, J.; Hou, F. J.; Chen, Y. C.; Chen, H. M.; Yang, S. P.; Cheng, C. C.; Chen, H. L. Robust Airlike Superhydrophobic Surfaces. *Adv. Mater.* **2010**, *22*, 597−601.
(36) Yildirim, A.; Budunoglu, H.; Daglar, B.; Deniz, H.; Bayindir, M. One-Pot Preparation of Fluorinated Mesoporous Silica Nanoparticles for Liquid Marble Formation and Superhydrophobic Surfaces. *ACS Appl. Mater. Interfaces* **2011**, *3*, 1804−1808.
(37) Chantarak, S.; Chang, J.; Suwanboon, S.; Riyajan, S. One-Pot Synthesis of Ultrahydrophobic Mesoporous Silica Nanoparticles. *Mater. Res. Express* **2018**, *5*, No. 095030.
(38) Jin, Q.; Lin, C. Y.; Kang, S. T.; Chang, Y. C.; Zheng, H.; Yang, C. M.; Yeh, C. K. Superhydrophobic Silica Nanoparticles as Ultrasound Contrast Agents. *Ultrason. Sonochem.* **2017**, *36*, 262−269.
(39) Ye, H.; Zhu, L.; Li, W.; Liu, H.; Chen, H. Constructing Fluorine-Free and Cost-Effective Superhydrophobic Surface with Normal-Alcohol-Modified Hydrophobic SiO_2 nanoparticles. *ACS Appl. Mater. Interfaces* **2017**, *9*, 858−867.
(40) Ogihara, H.; Xie, J.; Okagaki, J.; Saji, T. Simple Method for Preparing Superhydrophobic Paper: Spray-Deposited Hydrophobic Silica Nanoparticle Coatings Exhibit High Water-Repellency and Transparency. *Langmuir* **2012**, *28*, 4605−4608.
(41) Anitha, C.; Azim, S. S.; Mayavan, S. Fluorine Free Superhydrophobic Surface Textured Silica Particles and Its Dynamics e Transition from Impalement to Impingement. *J. Alloys Compd.* **2017**, *711*, 197−204.
(42) Gu, H.; Zhang, Q.; Gu, J.; Li, N.; Xiong, J. Facile Preparation of Superhydrophobic Silica Nanoparticles by Hydrothermal-Assisted Sol−Gel Process and Effects of Hydrothermal Time on Surface Modification. *J. Sol−Gel Sci. Technol.* **2018**, *87*, 478−485.

https://doi.org/10.1021/acsanm.1c00398
ACS Appl. Nano Mater. 2021, 4, 4092−4102

(43) Li, X.; Cao, Z.; Liu, F.; Zhang, Z.; Dang, H. A Novel Method of Preparation of Superhydrophobic Nanosilica in Aqueous Solution. *Chem. Lett.* **2006**, *35*, 94−95.
(44) Santiago, A.; González, A.; Iruin, J. J.; Fernández-Berridi, M. J.; Irusta, L. Preparation of Superhydrophobic Silica Nanoparticles by Microwave Assisted Sol-Gel Process. *J. Sol−Gel Sci. Technol.* **2012**, *61*, 8−13.
(45) Brassard, J. D.; Sarkar, D. K.; Perron, J. Synthesis of Monodisperse Fluorinated Silica Nanoparticles and Their Superhydrophobic Thin Films. *ACS Appl. Mater. Interfaces* **2011**, *3*, 3583−3588.
(46) Xu, Q. F.; Wang, J. N.; Sanderson, K. D. Organic-Inorganic Composite Nanocoatings with Superhydrophobicity, Good Transparency, and Thermal Stability. *ACS Nano* **2010**, *4*, 2201−2209.
(47) Li, X.; Du, X.; He, J. Self-Cleaning Antireflective Coatings Assembled from Peculiar Mesoporous Silica Nanoparticles. *Langmuir* **2010**, *26*, 13528−13534.
(48) Lee, Y.-G.; Park, J.-H.; Oh, C.; Oh, S.-G.; Kim, Y. C. Preparation of Highly Monodispersed Hybrid Silica Spheres Using a One-Step Sol−Gel Reaction in Aqueous Solution. *Langmuir* **2007**, *23*, 10875−10878.
(49) Hu, T.-M.; Chou, H.-C.; Lin, C.-Y. Facile Green Synthesis of Organosilica Nanoparticles by a Generic "Salt Route.". *J. Colloid Interface Sci.* **2019**, *539*, 634−635.
(50) Bogush, G. H.; Zukoski, C. F., IV Studies of the Kinetics of the Precipitation of Uniform Silica Particles through the Hydrolysis and Condensation of Silicon Alkoxides. *J. Colloid Interface Sci.* **1991**, *142*, 1−18.
(51) Carcouët, C. C. M. C.; van de Put, M. W. P.; Mezari, B.; Magusin, P. C. M. M.; Laven, J.; Bomans, P. H. H.; Friedrich, H.; Esteves, A. C. C.; Sommerdijk, N. A. J. M.; van Benthem, R. A. T. M.; de With, G. Nucleation and Growth of Monodisperse Silica Nanoparticles. *Nano Lett.* **2014**, *14*, 1433−1438.
(52) Han, Y.; Lu, Z.; Teng, Z.; Liang, J.; Guo, Z.; Wang, D.; Han, M. Y.; Yang, W. Unraveling the Growth Mechanism of Silica Particles in the Stöber Method: In Situ Seeded Growth Model. *Langmuir* **2017**, *33*, 5879−5890.
(53) Giasuddin, A. B. M.; Britt, D. W. Monitoring Silane Sol-Gel Kinetics with in-Situ Optical Turbidity Scanning and Dynamic Light Scattering. *Molecules* **2019**, *24*, No. 2931.
(54) Rios, X.; Moriones, P.; Echeverría, J. C.; Luquin, A.; Laguna, M.; Garrido, J. J. Ethyl Group as Matrix Modifier and Inducer of Ordered Domains in Hybrid Xerogels Synthesised in Acidic Media Using Ethyltriethoxysilane (ETEOS) and Tetraethoxysilane (TEOS) as Precursors. *Mater. Chem. Phys.* **2013**, *141*, 166−174.
(55) Dong, F.; Xie, H.; Zheng, Q.; Ha, C. S. Superhydrophobic Polysilsesquioxane/Polystyrene Microspheres with Controllable Morphology: From Raspberry-like to Flower-like Structure. *RSC Adv.* **2017**, *7*, 6685−6690.
(56) Yaoke, D.; Yuan, Z.; Wang, J. Synthesis of a Phosphorus-Containing Trisilanol POSS and Its Application in RTV Composites. *E-Polymers* **2018**, *18*, 237−245.
(57) Orel, B.; Ješe, R.; Vilčnik, A.; Štangar, U. L. Hydrolysis and Solvolysis of Methyltriethoxysilane Catalyzed with HCl or Trifluoroacetic Acid: IR Spectroscopic and Surface Energy Studies. *J. Sol−Gel Sci. Technol.* **2005**, *34*, 251−265.
(58) Lei, X. F.; Qiao, M. T.; Tian, L. D.; Yao, P.; Ma, Y.; Zhang, H. P.; Zhang, Q. Y. Improved Space Survivability of Polyhedral Oligomeric Silsesquioxane (POSS) Polyimides Fabricated via Novel POSS-Diamine. *Corros. Sci.* **2015**, *90*, 223−238.
(59) Nallathambi, G.; Ramachandran, T.; Rajendran, V.; Palanivelu, R. Effect of Silica Nanoparticles and BTCA on Physical Properties of Cotton Fabrics. *Mater. Res.* **2011**, *14*, 552−559.
(60) Rios, X.; Moriones, P.; Echeverría, J. C.; Luquín, A.; Laguna, M.; Garrido, J. J. Characterisation of Hybrid Xerogels Synthesised in Acid Media Using Methyltriethoxysilane (MTEOS) and Tetraethoxysilane (TEOS) as Precursors. *Adsorption* **2011**, *17*, 583−593.
(61) Launer, J. P. Infrared Analysis of Organosilicon Compounds: Spectra-Structure Correlations, Silicon compounds: silanes & silicones, 2013, https://www.gelest.com/wp-content/uploads/5000A_Section1_InfraredAnalysis.pdf.
(62) Lenza, R. F. S.; Vasconcelos, W. L. Structural Evolution of Silica Sols Modified with Formamide. *Mater. Res.* **2001**, *4*, 175−179.
(63) Suegama, P. H.; Aoki, I. V. Electrochemical Behavior of Carbon Steel Pre-Treated with an Organo Functional Bis-Silane Filled with Copper Phthalocyanine. *J. Braz. Chem. Soc.* **2008**, *19*, 744−754.
(64) Baatti, A.; Erchiqui, F.; Bébin, P.; Godard, F.; Bussières, D. A Two-Step Sol-Gel Method to Synthesize a Ladder Polymethylsilsesquioxane Nanoparticles. *Adv. Powder Technol.* **2017**, *28*, 1038−1046.
(65) Park, E. S.; Ro, H. W.; Nguyen, C. V.; Jaffe, R. L.; Yoon, D. Y. Infrared Spectroscopy Study of Microstructures of Poly(Silsesquioxane)S. *Chem. Mater.* **2008**, *20*, 1548−1554.
(66) Viart, N.; Niznansky, D.; Rehspringer, J. L. Structural Evolution of a Formamide Modified Sol - Spectroscopic Study. *J. Sol−Gel Sci. Technol.* **1997**, *8*, 183−187.
(67) Fidalgo, A.; Ilharco, L. M. The Defect Structure of Sol-Gel-Derived Silica/Polytetrahydrofuran Hybrid Films by FTIR. *J. Non-Cryst. Solids* **2001**, *283*, 144−154.
(68) Chmel, A.; Mazurina, E. K.; Shashkin, V. S. Vibrational Spectra and Deffect Structure of Silica Prepared by Non-Organic Sol-Gel Process. *J. Non-Cryst. Solids* **1990**, *122*, 285−290.
(69) Pereira, C.; Alves, C.; Monteiro, A.; Magén, C.; Pereira, A. M.; Ibarra, A.; Ibarra, M. R.; Tavares, P. B.; Araújo, J. P.; Blanco, G.; Pintado, J. M.; Carvalho, A. P.; Pires, J.; Pereira, M. F. R.; Freire, C. Designing Novel Hybrid Materials by One-Pot Co-Condensation: From Hydrophobic Mesoporous Silica Nanoparticles to Superamphiphobic Cotton Textiles. *ACS Appl. Mater. Interfaces* **2011**, *3*, 2289−2299.
(70) Sim, L. N.; Majid, S. R.; Arof, A. K. FTIR Studies of PEMA/PVdF-HFP Blend Polymer Electrolyte System Incorporated with $LiCF_3SO_3$ Salt. *Vib. Spectrosc.* **2012**, *58*, 57−66.
(71) Nagesetti, A.; McGoron, A. J. Multifunctional Organically Modified Silica Nanoparticles for Chemotherapy, Adjuvant Hyperthermia and near Infrared Imaging. *Colloids Surf., B* **2016**, *147*, 492−500.

https://doi.org/10.1021/acsanm.1c00398
ACS Appl. Nano Mater. 2021, 4, 4092−4102